

Label-free imaging of fibroblast membrane interfaces and protein signatures with vibrational infrared photothermal and phase signals

PANAGIS D. SAMOLIS,^{1,2} DANIEL LANGLEY,^{3,4} BREANNA M. O'REILLY,^{5,6} ZAY OO,^{3,4} GEVA HILZENRAT,^{3,4} SHYAMSUNDER ERRAMILLI,^{2,7,8} ALLYSON E. SGRO,^{5,6,7} SALLY MCARTHUR,^{3,4} AND MICHELLE Y. SANDER^{1,2,5,8,*} 

¹Department of Electrical and Computer Engineering, Boston University, Boston, MA 02215, USA

²Photonics Center, Boston University, Boston, MA 02215, USA

³Bioengineering Research Group Engineering and Technology, Faculty of Science, Engineering and Technology, Swinburne University of Technology, Hawthorn, Victoria, Australia

⁴Biomedical Manufacturing, CSIRO Manufacturing, Melbourne, VIC, Australia

⁵Department of Biomedical Engineering, Boston University, Boston, MA 02215, USA

⁶Biological Design Center, Boston University, Boston, MA 02215, USA

⁷Department of Physics, Boston University, Boston, MA 02215, USA

⁸Division of Materials Science and Engineering, Boston University, Brookline, MA 02446, USA

*msander@bu.edu

Abstract: Label-free vibrational imaging of biological samples has attracted significant interest due to its integration of structural and chemical information. Vibrational infrared photothermal amplitude and phase signal (VIPPS) imaging provide label-free chemical identification by targeting the characteristic resonances of biological compounds that are present in the mid-infrared fingerprint region (3 μm - 12 μm). High contrast imaging of subcellular features and chemical identification of protein secondary structures in unlabeled and labeled fibroblast cells embedded in a collagen-rich extracellular matrix is demonstrated by combining contrast from absorption signatures (amplitude signals) with sensitive detection of different heat properties (lock-in phase signals). We present that the detectability of nano-sized cell membranes is enhanced to well below the optical diffraction limit since the membranes are found to act as thermal barriers. VIPPS offers a novel combination of chemical imaging and thermal diffusion characterization that paves the way towards label-free imaging of cell models and tissues as well as the study of intracellular heat dynamics.

© 2020 Optical Society of America under the terms of the [OSA Open Access Publishing Agreement](#)

1. Introduction

Imaging complex biological samples and biomimetic tissue cultures is of great interest to life scientists [1]. Fluorescence microscopy techniques such as confocal and multiphoton have demonstrated high specificity and unique super-resolution capabilities [2]. However, there is a need to identify novel non-invasive label-free imaging modalities that do not rely on exogenous staining of cells to provide contrast. Biological molecules present in cells and tissues, including proteins, lipids and nucleic acids, have strong characteristic vibrational resonances in the molecular fingerprint region (the mid-infrared wavelength regime from 3–12 μm). While chemical content can be measured with Raman based techniques, e.g. Coherent Raman microscopy [3–5], the conventional Raman scattering cross-sections are lower than the corresponding infrared absorption cross-sections by around ten orders of magnitude [6]. Thus, infrared (IR) absorption based imaging methods, like FTIR, promise high sensitivity for chemical imaging [7–9]. However,

due to the large diffraction limited spot sizes of mid-infrared (mid-IR) beams the spatial resolution of conventional IR is around 5–12 μm , making the imaging of subcellular features challenging [10].

Mid-infrared photothermal microscopy targets the infrared absorption cross-section and has recently shown unique capabilities for cell imaging with spatial resolution down to sub-micron values [11,12] while providing chemical information [11–14]. Depth-resolved imaging [11] as well as the capability to detect features as small as 50 nm [15], smaller than the probe diffraction limit due to thermal expansion and diffusion, has been demonstrated. Different biomedical applications of mid-infrared photothermal microscopy explored e.g. in vivo imaging in *C. elegans* [11], live cell imaging of cellular dynamics in neurons and oligodendrocytes [13], and super resolution imaging of polymorphic amyloid aggregates in neurons [14]. Multi-modular imaging approaches have led to the combination of IR and optical microscopy [16], bond selective transient phase imaging [17] and ultrafast widefield imaging of live cells [18] with vibrational sensitivity. Recently, a mid-infrared photothermal was combined with quantitative phase imaging approaches [19] including digital holography and optical diffraction holography [20], which allowed depth-resolved quantitative phase imaging of live cells. IR microscopy has also been merged with atomic force microscopy (AFM-IR) to study eukaryotic cells [21] with resolving powers down to 120 nm. While significant progress has been made [6,13,22], chemical mid-IR photothermal imaging for biomedical applications has been demonstrated using mostly visible probe beams and thus has been limited to unlabeled biological samples. Therefore, a direct validation with fluorescently labeled cells has not been conducted. Further, for mid-infrared photothermal studies, the focus has been mostly on the photothermal amplitude signal, while the rich information from the photothermal lock-in phase has not been evaluated in detail. We will present that by analyzing the lock-in phase signal, related to thermal diffusion properties [23,24], differentiation of features with overlapping vibrational signatures is facilitated, that are otherwise challenging to get resolved. Due to similar absorption properties between intracellular and extracellular matrix proteins, there are currently few IR studies undertaken on tissue engineered models, in which cells are grown in two and three dimensional extracellular matrices. The latter are important models that replicate human physiology [1] and can be used to study cellular functions including proliferation, growth, and response to external stimuli. However, biochemical characterization of cancer-activated fibroblast cells with FTIR spectroscopy [25] have been performed only on isolated cells grown directly on IR transparent windows. Other label-free infrared absorption studies focused on fibroblast cells grown directly on a CaF_2 windows [6,10].

In this paper, we present Vibrational Infrared Photothermal and Phase Signal (VIPPS) imaging to map the protein distribution in fibroblast cells grown in a collagen matrix as a physiologically relevant model. By simultaneously mapping changes in absorption as well as thermal diffusion rates, high contrast from features with different thermal diffusivity but overlapping absorption profiles can be obtained [24], creating an opportunity to evaluate this approach in tissue models. Utilizing the increased thermal resistivity observed at membrane structures, VIPPS offers high contrast from the plasma and nuclear membrane of cells and the capability to detect biological boundaries, well below the diffraction limit. We identify areas of protein accumulation of higher order secondary conformations at the subcellular level and study how their presence affects heat transport across membrane structures. For validation, we analyze fluorescently labeled and unlabeled cells, making this a platform directly compatible with existing state-of-the-art microscopy tools. Overall, VIPPS enables simultaneous study of chemical composition combined with thermal diffusion dynamics that can offer diverse and enriching insights into cell growth and structure as well as intracellular heat dynamics.

2. VIPPS microscope

This label-free microscope utilizes the photothermal effect to translate the mid-IR vibrational response to a shorter wavelength continuous wave (CW) probe beam in the near infrared at $1.5\ \mu\text{m}$. A pulsed quantum cascade laser (QCL, Daylight Solutions) with a tunable range from $1580\ \text{cm}^{-1}$ - $1740\ \text{cm}^{-1}$, serves as the pump beam. The repetition rate is set at 100 kHz with pulse durations at 500 ns. The probe and pump beam are combined by a dichroic mirror (DM) before entering a ZnSe objective (numerical aperture NA=0.25) and focused on the sample. The diffraction limited spot sizes of the pump and probe beam are estimated around $12\ \mu\text{m}$ and $3.1\ \mu\text{m}$. The induced modulation of the refractive index due to thermal heating is also referred to as a thermal lens [26]. As illustrated in Fig. 1, the probe beam experiences periodic scattering as it passes through the sample due to the modulated thermal lensing effect. The transmitted probe beam is collected in a heterodyne measurement [27] and focused on an InGaAs photodetector (PD). The photodetector signal is connected to a lock-in amplifier (Zurich Instruments) after a 50X pre-amplification. The lock-in amplifier is synchronized to the pump reference and is used to extract the photothermal amplitude signal PTS, which is proportional to the induced absorption and heat-induced refractive index change.

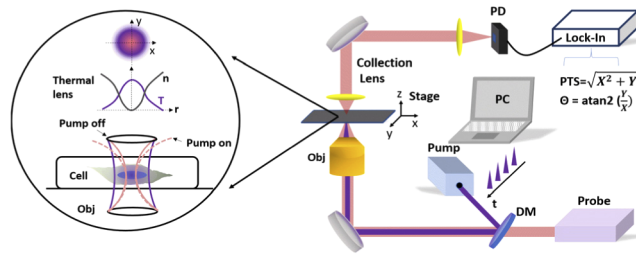


Fig. 1. Experimental setup of the VIPPS mid-infrared photothermal microscope. The pulsed quantum cascade laser (pump) is co-aligned with a near infrared laser (probe) and co-focused on the sample with a ZnSe objective (Obj). The zoom-in illustrates the build-up of a thermal lens in the sample. The modulated forward scatter of the probe laser is detected in a heterodyne measurement on a photodetector (PD) with a lock-in amplifier (Lock-In) and separated into a photothermal amplitude PTS and phase signal Θ .

For imaging of protein signatures the wavenumber is tuned to the corresponding molecular bonds of the Amide-I band at $1660\ \text{cm}^{-1}$. To image fluorescently labeled and non-labeled cells, the use of a probe beam in the near infrared is beneficial to avoid the visible regime with absorption and emission of the exogenous stains. Residual absorption at the probe wavelength can be neglected since the absorption coefficient of collagen at $1660\ \text{cm}^{-1}$ is by a factor 1000 to 10000 higher than the absorption coefficient at $1.5\ \mu\text{m}$ [28,29]. In addition, based on the lock-in principle any change in the CW probe power due to scattering or absorption from the probe is automatically filtered out so that mostly intensity noise fluctuations at 100 kHz can potentially contribute. However, these fluctuations on the order of $10\text{--}20\ \mu\text{V}$ (background noise when the pump laser is turned off) is regarded negligible compared to the obtained photothermal signal, which is on the order of tens of mV (when the pump laser is turned on). Further, transmission measurements of the overall CW probe power showed no significant power reduction upon propagation through the sample. The probe power focused on the sample is around 1 mW while the pump beam power on the sample amounts up to 3.5 mW at a wavenumber of $1660\ \text{cm}^{-1}$, below any potential tissue damage threshold. Imaging was performed by raster scanning through a field of view of interest with a variable step size of $1\ \mu\text{m}$ for the images that have a $80\ \mu\text{m}$ by $80\ \mu\text{m}$ FOV (field of view) or a $50\ \mu\text{m}$ by $100\ \mu\text{m}$ FOV. For higher resolution images with smaller

FOV of 15 μm by 15 μm or 20 μm by 15 μm , a 0.1 μm step size was used. For all images the pixel dwell time was at 90 ms, which was slightly longer than the integration time constant of 71 ms.

Unlike in other photothermal configurations, in VIPPS imaging the lock-in phase signal Θ is simultaneously extracted, which has been reported to be independent on absorption and solely related to the rate of heat transport [23]. Specifically the phase output is calculated as $\Theta = \text{atan2}(\frac{Y}{X})$, where X and Y are the in-phase and out-of-phase signals, respectively. The amplitude output is calculated as $PTS = \sqrt{X^2 + Y^2}$, which is always positive and proportional to the amount of absorption, while Θ has a dynamic range from $-\pi$ to π . It has been previously discussed that the physical origin of the out-of-phase signal Y in photothermal measurements is due to effects of thermal diffusion [23]. While the values of Y and X are both proportional to the increase or decrease of the scattering cross sections due to heating, their ratio is independent of the induced absorption and measures the relative contribution of thermally diffused signal Y with respect to the in-phase signal X . This is determined by the localized thermal resistance and the rate of heat transport (thermal diffusivity) and can take both positive and negative values, based on whether the thermal lensing causes the beam to focus or defocus [30]. In addition, points where the phase reaches 0 rad, (where $Y \ll X$), have been related to slow rates of heat transport and minimal thermal blurring [24]. Thus simultaneous acquisition of the photothermal amplitude and lock-in phase offers not only insights into the vibrational molecular bond structure but also thermal diffusion properties. Lock-in phase imaging has enabled imaging of absorbing features in an absorbing embedding medium based on their inherently different thermal diffusion values. Thus, 1 μm melamine beads embedded in an absorbing 8CB liquid crystal medium have been imaged with VIPPS microscopy, indicating an 8 fold improvement in spatial resolution, due to its high sensitivity in detecting changes in thermal diffusion [24].

3. VIPPS imaging of fibroblast cells in collagen and cross registration of sub-cellular features with fluorescence imaging

In Fig. 2, VIPPS imaging of fluorescently labeled and unlabeled fibroblast cells grown on a collagen extracellular matrix is demonstrated. (The sample preparation details can be found in the section on Materials and Methods in Supplement 1.) We focus on the Amide I band whose spectral signature arises from the C = O stretching vibrations from the amide groups of the peptide bonds. Brightfield images of a pair of unlabeled and labeled mouse fibroblast cells grown in the same matrix, are shown in Figs. 2(a) and 2(b), respectively. The corresponding PTS and fluorescence images of the two cells are shown in Figs. 2(c), 2(d), and in Figs. 2(e) and 2(f), respectively. An Andor Dragonfly Spinning Disk Confocal microscope was used for the fluorescent imaging. In the fluorescence image of the labeled cell, the overlap of the two channels corresponding to the nucleus and cytoplasm markers are shown in red and green [see Fig. 2(f)]. The DIC image of the labeled cell is shown in Fig. 2(g). Along with the PTS image of the labeled cell, the Θ image, shown in Fig. 2(h), is simultaneously acquired. Good agreement between features sizes from the VIPPS and fluorescent microscope is shown in the overlap image in Fig. 2(i), indicating a clear cross registration of the cell shape and nucleus size. While in the fluorescence image, the extending collagen fibrils are clearly visible, they are not fully reproduced in the PTS image, probably due to the different depth plane at which the fibrils exist compared to the main cell body. While the extracellular matrix and cell cytoplasm are characterized by similar PTS strength, stemming from the collagen environment and the produced collagen, the cell body can be clearly differentiated by the reduction in the PTS signal close to the outer cell structure. Similarly, a clear demarcation of the nucleus due to a drop in the PTS strength near the nuclear membrane is observed. The measured PTS is reduced by a factor of 28 and 8.8 to values of 0.8 ± 0.1 mV and 2.5 ± 0.15 mV near the cell plasma and nucleus interface, respectively. It should be noted that even though the values at membrane areas are small they reside significantly above the noise level (~ 20 μV) by at least a factor of 40. Thus, the corresponding SNR varies in

those areas has a range between 40 and 125, whereas in other parts of the sample with amplitudes up to 22.3 mV, the SNR increases up to 1115.

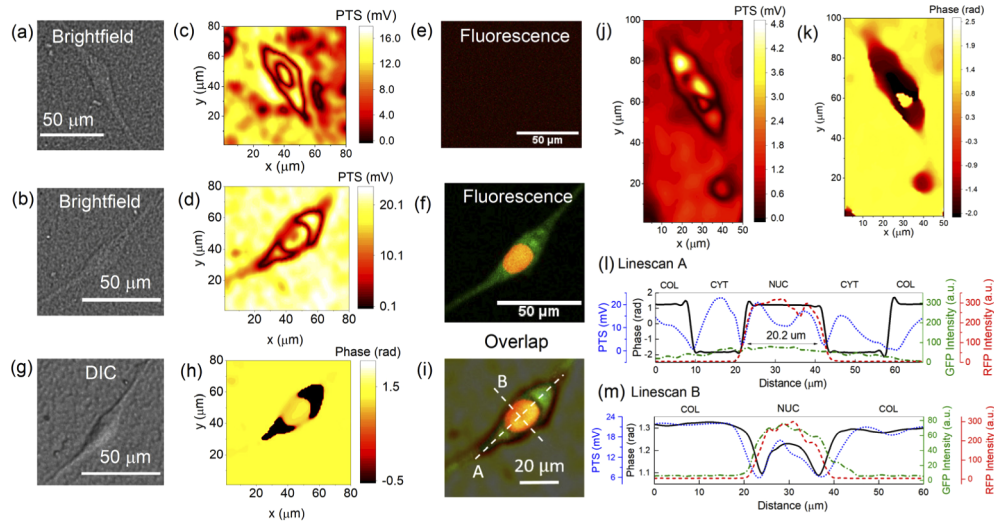


Fig. 2. Cross registration of VIPPS imaging of collagen embedded fibroblast cells with other imaging modalities. Brightfield images of (a) unlabeled mouse fibroblast cell grown in rat collagen and (b) labeled mouse fibroblast cell. PTS images of (c) unlabeled and (d) labeled cell at 1660 cm^{-1} . Fluorescence images of (e) unlabeled cell (no signal) and of (f) labeled cell (GFP in green and nucleus RFP in red). (g) DIC image of labeled cell. (h) Θ image of labeled cell. (i) Overlap between PTS and fluorescence image with linescan cross-sections A and B. (j) PTS and (k) Θ image of unlabeled human cell. (l) Linescan A and (m) B across cell obtained from PTS (dotted blue), Θ (solid black), RFP fluorescence (dashed red), GFP fluorescence (dash-dot green) showing straightforward cross registration and agreement of RFP and Θ signal in determining the cell nucleus dimension.

The decrease in PTS in the vicinity of the plasma and nucleus membrane corresponds to steep shifts in the measured lock-in phase. When transitioning from the collagen to the cytoplasm and similarly from the cytoplasm to the nucleus, Θ varies from 1.2 ± 0.01 rad to -1.8 ± 0.01 rad, as seen in Fig. 2(h). Similar effects for the PTS and Θ are observed in a separate sample consisting of human unlabeled fibroblast cells grown in rat tail collagen, see Figs. 2(j) and 2(k). In this sample, the PTS signal at the extracellular environment is lower in some areas of the intracellular environment. In both cases, while the PTS signal in the collagen and parts of the intracellular environment are both strong, the corresponding Θ signal shows a marked difference between the cytoplasm (CYT) and extracellular matrix (COL) providing high contrast from the outer cell boundaries. Equally high contrast is provided between the cell cytoplasm (CYT) and the nucleus (NUC) offering clear localization of the cell nucleus boundary. In other words, we find that the phase changes abruptly only near the membrane interfaces, implying a change in the rate of heat transport and a non-homogeneous distribution of heat across the interface (between the intra and extracellular environment or equivalently between the cytoplasm and nucleus environment). Hence, the property of Θ to be independent of absorption and sensitive to changes in the rate of heat transport allows us to identify the cell outer and nucleus boundary with high confidence.

With two linescans across the labeled mouse cell, linescan A, Fig. 2(i) and linescan B, Fig. 2(i), the performance between the VIPPS and fluorescent microscope are directly compared in Fig. 2(l) and Fig. 2(m). The evolution of the PTS signal (dotted blue) and Θ signal (solid black) are presented together with signals from the red fluorescent protein (RFP, dashed red) and green

fluorescent protein (GFP, dashed dotted green). Linescan A extends over the collagen, intracellular cytoplasm as well as the nucleus. The increase in Θ close to the nuclear membrane overlaps well with the increase in the RFP fluorescence signal. The width of the nucleus measured from the Θ linescan at 20.2 μm agrees very well with the full-width at half-maximum (FWHM) of the RFP fluorescence signal for the nucleus $\sim 20 \mu\text{m}$. In addition, the width measured from the PTS signal (defined as the distance between the locations of minima near the nucleus) also correlates with this data. Overall, Θ allows a clearer identification of the boundaries between the cytoplasm and collagen as well as between the cytoplasm and nucleus, see Fig. 2(l). The transitions are characterized by a steeper slope in Θ than for the PTS so that the differentiation of subcellular structures is enhanced compared to standard amplitude measurements. The signal from linescan B, vertical with respect to the cell orientation captured in Fig. 2(m), features a 3.5 times decrease in PTS (blue) and a 1.3 times decrease in phase Θ (black) at the collagen and nucleus boundary. The FWHM of the cell nucleus is measured to be close to 13.7 μm based on the RFP signal, while the separation of minimum signal points from both the PTS and Θ linescans corresponds to 12.7 μm , which is close to the FWHM from the RFP fluorescent signal. These results confirm that regardless of whether the cell is labeled or unlabeled, our VIPPS microscope can provide images of subcellular features in both human and mouse fibroblasts. A direct cross-registration between fluorescent microscopy and photothermal IR imaging on the same cell is thus demonstrated. This can prove extremely attractive to obtain multiple images from different imaging modalities on the same sample, facilitating integration with existing diagnostic approaches.

4. Contrast from varying thermal conductivity near membrane structures

Obtaining significant contrast from the absorption of biological structures in an embedded medium that features similar absorption properties can be challenging due to overlapping absorption bands and the potential masking of small features, as in the presented fibroblast cell. For the Amide-I protein absorption, both the intracellular and extracellular environment are expected to have a significant PTS signal contribution. In the following, the contrast C_{PTS} is defined as the PTS signal measured at the locations of interest (which includes the extracellular collagen, the cytoplasm and the cell nucleus) minus the minimum signal PTS_m (which can be found near the plasma or nuclear membrane) divided by the sum of the two signals as seen in Eq. (1). This value varies significantly but can reach up to 80.7% and 93.1% for both the labeled and unlabeled cell grown on the same sample.

$$C_{\text{PTS}} = \frac{\text{PTS} - \text{PTS}_m}{\text{PTS} + \text{PTS}_m} \quad (1)$$

While the cell cytoplasm is mainly composed of water ($\sim 80\%$), the second major constituent are proteins ($\sim 15\%$) with 95% of cellular proteins equally concentrated within the nucleus and cytoplasm [31], which explains the strong photothermal amplitude signal in both cell regions. Close to the plasma as well as nuclear membrane, both the photothermal amplitude and phase signal drop off significantly, offering a clear delineation and high contrast of these biological boundaries. The drop in PTS close to the membrane implies a reduction in signal originating from the Amide-I band and proteins in the vicinity. The cell membranes are primarily composed of phospholipid bilayers with integral and peripheral membrane proteins making up about 50% of their mass [32]. However, the membrane area inherently features a much lower absorption than its surroundings and thus a lower initial temperature increase (estimated to be at least 3 orders of magnitude lower). As a result, close to the plasma and nuclear membrane, the photothermal amplitude signal drops off significantly, implying a reduction in signal originating from the Amide-I band and proteins in the vicinity and offering a clear delineation and high contrast of these biological boundaries. The spatial imaging resolution of the system is determined by the convolution of the feature size with the diffraction-limited spot size of the probe beam (about 3.1 μm diameter in our system) combined with effects of thermal blurring related to

the thermal diffusivity of the sample. It was previously shown that the induced thermal spot can be larger than the object size due to thermal diffusion effects [24] so that as long as the signal is higher than the detection limit of the system, sub-diffraction limited features can be captured [15,33]. As discussed in [15,33], the contributions of a material's thermal expansion and thermo-optic coefficients can lead to such imaging contrast. In this work, despite the nano-meter sized dimensions of the membranes (as small as ~ 4 nm, much smaller than the probe beam diffraction limited spot size), the increased thermal resistivity of the membrane structures leads to a photothermal gradient at the interface that provides enhanced contrast and localization of features. The dip in the PTS signal at the membrane interface, raster-scanned with a step size of $0.1 \mu\text{m}$ in Fig. 2(d), has a spatial width around $3.1 \mu\text{m}$, which matches the system's resolution limitations. However, higher localization of these boundaries is achieved in the phase signal, see Fig. 2(h). The sharp change in phase overlaps with a steep shift in the derivative of the PTS signal $\frac{dPTS}{dx}$ across that interface. Thus, the presence of a strong temperature gradient profile and the thermal diffusion effects associated with the membrane environment allows capturing these boundaries with high contrast.

Similarly, the contrast C_Θ can be defined for the phase signal as the difference between the phase Θ of interest minus the minimized phase Θ_m divided by their sum, as seen in Eq. (2). Because Θ_m is minimized and approaches 0 rad near the membranes, C_Θ approaches 1 near the membrane crossings. The high contrast obtained in the lock-in phase signal Θ relies purely on changes in the rate of heat transport and is independent of varying absorption or concentration [24]. Unlike the PTS signal that can vary up to 60% in the cytoplasm or nucleus area away from the membrane, the lock-in phase Θ remains constant throughout and only shifts at these biological boundaries. Thus, areas contained by membranes with different thermal diffusion properties provide higher contrast and localization in the phase signal Θ .

$$C_\Theta = \frac{\Theta - \Theta_m}{\Theta + \Theta_m} \quad (2)$$

5. Spectral evolution of the secondary protein conformation near the nuclear membrane

To study the signal variations observed near membrane structures in more detail, the boundary area between the cell nucleus and cytoplasm of $15 \mu\text{m}$ by $15 \mu\text{m}$ was imaged, as shown in Fig. 3(a). PTS spectra corresponding to the Amide-I band, from 1580 – 1720 cm^{-1} , were collected at the cell nucleus (solid black), cytoplasm (solid green) and extracellular collagen (solid red), see Fig. 3(b), featuring a very similar shape with a peak close to 1660 cm^{-1} and a FWHM width $\sim 59 \text{ cm}^{-1}$. Multiple spectra capturing the transition from the nucleus through the nuclear membrane to the nearby cytoplasm over a $2 \mu\text{m}$ cross-section were analyzed. Figure 3(c) shows the zoom-in of the region of interest, with the locations where spectra were collected marked by colored dots. The corresponding spectra are shown in Fig. 3(d). The first spectra collected near the nuclear membrane (Fig. 3(d) – purple trace) has a larger shoulder at the lower wavenumber regime between 1600 cm^{-1} and 1660 cm^{-1} , compared to spectra taken at the center of the nucleus. When crossing the nucleus membrane, the signal drops significantly by a factor of 6 accompanied by spectral shifts: The maximum signal is no longer centered at 1660 cm^{-1} , but shifts to lower wavenumbers, around 1625 cm^{-1} and 1605 cm^{-1} . As seen in Fig. 3(e) in the green and orange traces, the signal around 1625 cm^{-1} is 1.4 and 1.8 times higher than the signal at 1660 cm^{-1} , respectively. In addition, observed peaks at longer wavenumbers including 1696 cm^{-1} (Fig. 3(e) – green trace) and 1704.8 cm^{-1} (Fig. 3(e) – orange trace) are detected, which also have a higher signal than the PTS value at 1660 cm^{-1} by factors of 1.4 and 1.2, respectively. For locations close to the outer leaflet of the nuclear membrane closer to the cytoplasm, the peak gets recentered at 1660 cm^{-1} . These spectral shifts indicate changes in the chemical composition near the nuclear membrane that varies from other cell areas.

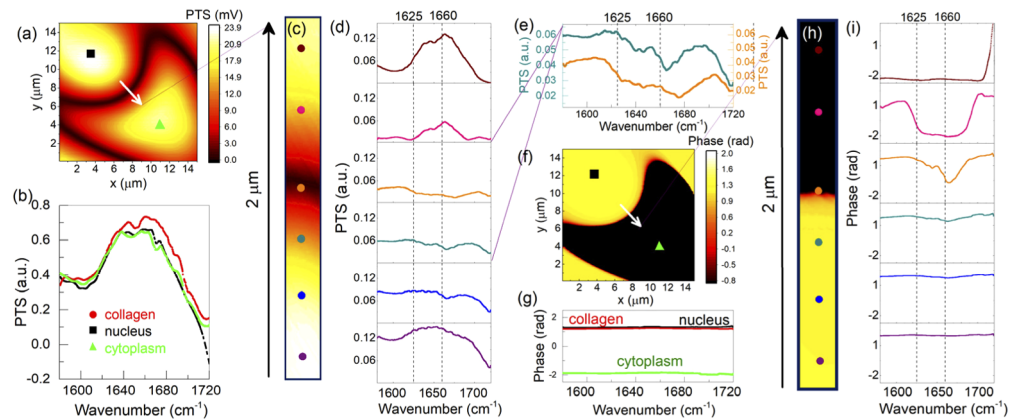


Fig. 3. VIPPS imaging of fluorescently labeled cell perinuclear area with spectral characterization: (a) PTS image of region near the cell nucleus at 1660 cm^{-1} , (b) PTS spectra taken at nucleus, collagen and cytoplasm, (c) Zoom-in PTS image of region near nucleus membrane boundary. (d) Evolution of PTS spectrum from nucleus (bottom) to cytoplasm (top) with spectra closest to the membrane in (e). (f) Corresponding Θ image. (g) The phase signal remains constant for each spectral region indicating a constant thermal diffusion rate. (h) Zoom-in Θ image of region near nucleus membrane with phase spectra shown in (i).

The Θ image of the same area is shown in Fig. 3(f). While the measured phase spectra Θ for the collagen and nucleus have similar values around 1.2 ± 0.01 , see Fig. 3(g), the value at the cytoplasm differs and is around -1.8 ± 0.01 rad, indicating different thermal diffusion properties. Overall, a relative homogeneous distribution of the underlying absorbing structure within the measured spot size is assumed and can account for such a flat phase across the measured wavelength region. The zoom-in of the Θ image of the region near the nuclear membrane is shown in Fig. 3(h) with the corresponding color-coded collected spectra in Fig. 3(i), corresponding to the same locations as for the PTS amplitude spectra in Fig. 3(d). Starting within the inner part of the nucleus at the bottom, the phase is constant at 1.12 rad. As the focal spot approaches the nuclear membrane, spectral phase shifts are observed, indicating different phase signatures for different wavenumber regions. For spectra taken near the nuclear membrane, multiple wavenumbers at which Θ crosses zero are detected (see Fig. 3(i) – orange trace), including at 1644.2 cm^{-1} and 1677.4 cm^{-1} . By moving the focal spot $0.2\text{ }\mu\text{m}$ (see Fig. 3(i) – red trace), the wavenumbers where Θ crosses zero shifts to the spectral wings at 1622.4 cm^{-1} and 1695.0 cm^{-1} . Eventually the phase stabilizes around a constant value of -1.73 rad at the location of the nucleus outer leaflet. The phase spectral shifts indicate a wavelength dependent modification in the heat transport dynamics, uniquely occurring near the nuclear and plasma membranes.

The Amide I vibrational band, aside from being one of the strongest resonant bands for proteins, is sensitive to the backbone protein conformation, since different structural conformations have different characteristic resonances. Different secondary protein structures are characterized by shifts in the peak in the vibrational spectrum: α -helices ($1656\text{--}1662\text{ cm}^{-1}$), side chains/aggregated strands ($1605\text{--}1615\text{ cm}^{-1}$), β -sheets ($1622\text{--}1627\text{ cm}^{-1}$, 1696 cm^{-1}), random coils ($1638\text{--}1646\text{ cm}^{-1}$) and β -turns ($1675\text{--}1685\text{ cm}^{-1}$) [34]. The collected PTS spectra can be regarded as a convolution of the individual spectral responses within the amide I band, each corresponding to a different conformation. Near the nuclear membrane, a rise of absorption peaks centered at 1625 cm^{-1} and 1605 cm^{-1} is observed, which corresponds to the bands for β -sheets and aggregated strands. Assuming shifts in the PTS spectrum stem pre-dominantly from variations in the secondary protein conformation, the ratio between the PTS amplitude at

1625 cm^{-1} and 1660 cm^{-1} , defined in Eq.(3), can be regarded representative for the accumulation of β -sheets versus α -helices.

$$\rho = \frac{\text{PTS}_{1625}}{\text{PTS}_{1660}} \quad (3)$$

Similar analysis based on similar spectroscopic amplitude ratios and data have been applied previously to study protein aggregates in neurological tissue [14] and to interpret vibrational and FTIR measurements [34,35]. To quantify the difference in the thermal diffusion rate for the two wavelengths corresponding to unique conformational spectral signatures, the phase difference is defined in Eq. (4).

$$\Delta\Theta = |\Theta_{1625} - \Theta_{1660}| \quad (4)$$

At the locations of the nucleus, collagen and cytoplasm ρ is comparable and equal to around 0.79. In addition, Θ is constant throughout the spectral region of interest, as indicated by $\Delta\Theta$ of 0 rad. When transitioning from the nucleus across the membrane interface, ρ starts to gradually increase from 0.79 to a maximum value of 1.75 while Θ_{1660} starts to decrease from 1.12 rad (at the nucleus center) to 0.68 rad. However, Θ_{1625} only decreases to 1.09 rad giving a notable phase difference $\Delta\Theta$ of 0.41 rad. As the focal spot moves closer to the cytoplasm, ρ decreases further down to 0.39 and the minimum value of 0.13, and $\Delta\Theta$ reaches a maximum value of 1.9 rad before decreasing again back to 0 rad when having reached the outer leaflet of the nuclear membrane. While ρ varies significantly at the perinuclear area, an increase in the absolute phase difference $\Delta\Theta$ is also reported, which suggests that the presence of secondary protein conformations affects the rate of heat transport. These effects are captured directly in linescans of ρ and $\Delta\Theta$ from the cell nucleus across the membrane boundary to the nearby cytoplasm, as shown in more detail in Fig. 4(a). We observe that for the spatial location where $\Theta_{1660} = 0$ rad, the ratio ρ reaches a maximum value of 1.69, while ρ reaches a minimum value of 0.19 when $\Theta_{1625} = 0$ rad.

Performing dual-spectral imaging enables us to localize the observed chemical changes in two dimensions. We obtain PTS images at 1625 cm^{-1} and 1660 cm^{-1} shown in Fig. 4(b) and Fig. 4(c), respectively. The corresponding Θ images are depicted in Figs. 4(d) and 4(e). By taking the ratio of the two PTS images, we obtain a ratio ρ image shown in Fig. 4(f), where enhancements are localized near the nuclear as well as the plasma membrane. In the 1 μm by 5 μm inset image of the nuclear membrane area localized changes in ρ feature amplitude variations of ± 0.2 . From the spectroscopic studies, we observe that the variations in ρ are accompanied by corresponding shifts in Θ . Thus the $\Delta\Theta$ image in Fig. 4(g) enhances areas with significant offsets in Θ . Here, localized signal fluctuations in $\Delta\Theta$ vary around ± 0.5 . Overall $\Delta\Theta$ images highlight spectral differences more finely than in ρ images and provide almost two times higher contrast and better localization of secondary protein structures.

Similar dual-spectral imaging and spectroscopy measurements were performed at the perinuclear area of the unlabeled human fibroblast cell (a 20 μm x 17 μm area at 1660 cm^{-1}), as seen in Fig. 5(a). The PTS spectra collected at the nucleus center (solid black), extracellular collagen (dashed dotted green) and cytoplasm (dashed red), share a peak at 1660 cm^{-1} , a FWHM close to 59 cm^{-1} , and a ρ value, around 0.7, see Fig. 5(b). In the spectra, shown in Fig. 5(b) (dotted orange), the peak is shifted from 1660 cm^{-1} to 1638 cm^{-1} . Here, the ratio ρ is equal to 1.16, which is higher than the value measured for the other cell areas of high protein content or in the outer collagen. For this cell a potential higher accumulation of β sheet proteins is located at the cytoplasm in the perinuclear area located at the upper side of the nucleus. Similarly to the labeled mouse cell, spectra closer to the membrane interface show clear shifts in the chemical composition, see Fig. 5(c), with a peak at the lower wavenumber region around 1625 cm^{-1} (dashed pink spectrum) and a ratio ρ around 2.15 in good agreement with the previous analysis in Fig. 4. When translating the focal spot 0.5 μm towards the nucleus, the measured spectrum shown in blue features an additional peak at 1660 cm^{-1} with a width of 32.8 cm^{-1} and a ratio ρ around 0.52. These variations in ρ around the membrane, both in terms of increase and decrease,

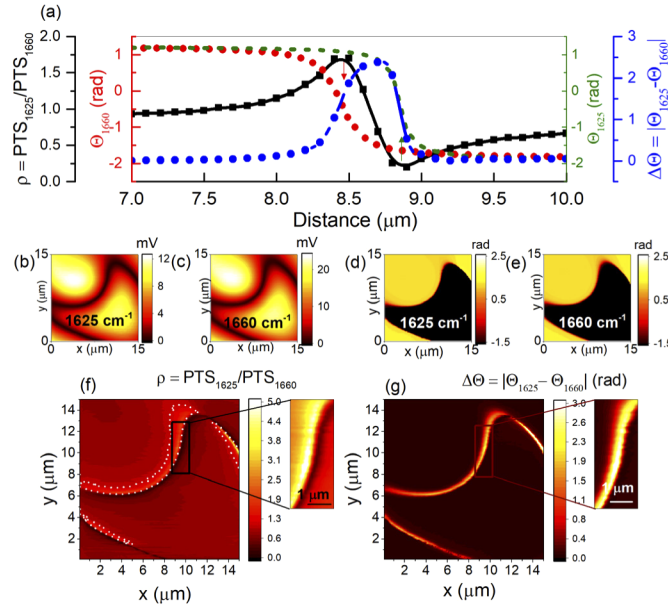


Fig. 4. Bi-spectral VIPPS imaging of labeled cell nucleus area. (a) Changes in the linescans highlight the nucleus membrane interface for Θ at 1660 cm^{-1} (dotted red) and at 1625 cm^{-1} (dashed green), for the ratio ρ (black square dots) and for $\Delta\Theta$ (blue circle dots). PTS image (b) at 1625 cm^{-1} and (c) at 1660 cm^{-1} . Θ image (d) at 1625 cm^{-1} and (e) at 1660 cm^{-1} . (f) Ratio PTS image $\rho = \text{PTS}_{1625} / \text{PTS}_{1660}$ where significant changes are localized at the nucleus membrane. (g) Difference Θ image $\Delta\Theta = |\Theta_{1660} - \Theta_{1625}|$, where significant changes are observed at the nucleus membrane with higher contrast.

compared to the standard value of 0.7 at locations of high protein content (including the collagen, nucleus center) agree with our previous measurements. To localize this accumulation of β sheet proteins further, we performed dual-spectral imaging at a wavelength of 1660 cm^{-1} as well as at 1625 cm^{-1} , with the corresponding ratio ρ image depicted in Fig. 5(d). The higher signal indicates an accumulation of β sheet signatures at the upper side of the perinuclear area (interface A) and a less pronounced accumulation at the lower side of the nuclear membrane (interface B) as well as in other areas near the plasma membrane. Similarly to our previous results, $\Delta\Theta$ peaks at areas characterized by a strong variation in ρ , see Fig. 5(e). The linescans in Fig. 5(f) show the evolution of the lock-in phase Θ at 1660 cm^{-1} (dotted red) and at 1625 cm^{-1} (dashed green), the ratio ρ (black square dots solid line) and the lock-in phase difference $\Delta\Theta$ image (blue circle dots solid line) across the two representative membrane interfaces A and B of the nucleus. The signal at 1625 cm^{-1} , potentially from an accumulation of β sheet proteins, is higher at interface A compared to B, by a factor of 4.1. In addition the FWHM of the $\Delta\Theta$ peak at interface A is larger than the one at B (1.8 μm compared to 0.6 μm). This indicates that the potential higher accumulation of β sheets near interface A results in a larger spatial phase shift and a more significant change in the rate of heat transport across the membrane interface.

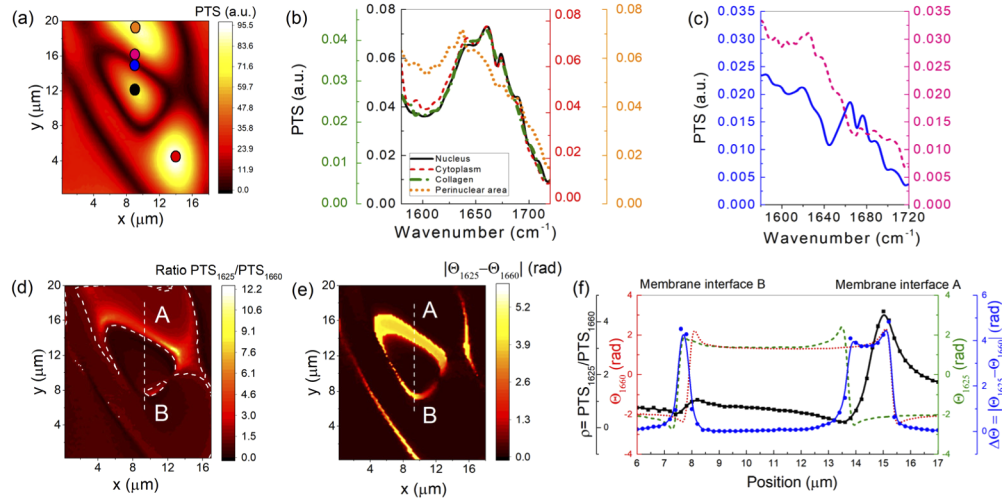


Fig. 5. Spectral VIPPS imaging of unlabeled human cell perinuclear area: (a) PTS image of cell nucleus area taken at 1660 cm^{-1} (b) PTS spectrum at cell nucleus (solid black), cytoplasm (dashed red) and collagen (dashed dotted green) and cytoplasm near perinuclear area (dotted orange). (c) Two neighboring PTS spectra (offset by $0.5\text{ }\mu\text{m}$ from each other) close to the nuclear membrane. (d) The ratio image $\rho = \text{PTS}_{1625}/\text{PTS}_{1660}$ can be indicative of higher β sheet protein accumulation on the top side of the nucleus. (e) The difference Θ image $\Delta\Theta = |\Theta_{1625} - \Theta_{1660}|$ enhances spectral phase shifts with a broader shift on the top side of the nucleus (area marked A). (f) The linescans across the nucleus membrane interface from Θ image at 1660 cm^{-1} (dotted red) and at 1625 cm^{-1} (dashed green), ρ image (black square dots) and $\Delta\Theta$ image (blue circle dots) show enhancements near the membrane interface areas.

6. Contrast from varying secondary protein conformation

Overall, the lock-in phase difference image provides a contrast $C_{\Delta\Theta}$ from the nuclear and plasma membrane boundaries as defined in Eq. (5), where $\Delta\Theta_m$ is the phase difference at the membrane, and $\Delta\Theta$ the baseline phase difference at the surrounding environment. This can reach values as high as 95.7% near the membrane interface of the mouse labeled fibroblast cell presented in Fig. 4. For the unlabeled human cell, $C_{\Delta\Theta}$ ranges from 99.7% and 95.3% at interfaces A and B respectively.

$$C_{\Delta\Theta} = \frac{\Delta\Theta_m - \Delta\Theta}{\Delta\Theta_m + \Delta\Theta} \quad (5)$$

The corresponding contrast C_ρ from the ratio PTS imaging is defined in Eq. (6), where ρ_m is the ratio at the membrane, and ρ the baseline ratio at the surrounding environment.

$$C_\rho = \frac{\rho_m - \rho}{\rho_m + \rho} \quad (6)$$

Specifically, the value of C_ρ is close to $\sim 43.9\%$ for the membrane interface of the labeled mouse fibroblast presented in Fig. 4. For the membrane interfaces of the unlabeled human fibroblast presented in Fig. 5, C_ρ ranges from 20.5% and 72.4% at interfaces A and B respectively. Overall contrast provided by phase difference imaging $C_{\Delta\Theta}$ is higher compared to contrast from ratio imaging C_ρ . Difference phase imaging offers an attractive methodology for locating and enhancing areas of interest with higher contrast and resolution.

7. Photothermal confinement parameter

To investigate the heat diffusion dynamics further, we analyze an analog to the respective parameter thermal diffusion, the Kapitza length [36]. The maximum spatial temperature gradient along an interface can be estimated by the maximum temperature difference, divided by the thermal diffusion length as defined in Eq. (7), where R_{th} corresponds to the thermal diffusion length [37].

$$\nabla T_{\max} \sim \frac{\Delta T_{\max}}{R_{th}} \quad (7)$$

For our measurements, we derive equivalently a photothermal confinement parameter L . The photothermal signal PTS is proportional to the localized induced temperature difference ΔT as seen in Eq. (8), where σ is the scattering cross section for the probe and $\frac{\partial n}{\partial T}$ the material's thermo-optic coefficient [33].

$$PTS \sim \frac{\partial \sigma}{\partial n} \cdot \frac{\partial n}{\partial T} \cdot \Delta T \quad (8)$$

We define L as the ratio of the maximum photothermal amplitude signal difference ΔPTS_{\max} (here occurring between the nuclear membrane region and the nearby cytoplasm) over the slope along the direction x across that transition $\partial PTS / \partial x$, defined in Eq. (9).

$$L = \frac{\Delta PTS_{\max}}{(\partial PTS / \partial x)} \quad (9)$$

From the PTS signal shown in Fig. 5(a), we calculate the value of L_{1660} for an excitation of 1660 cm^{-1} to be around $2.3 \text{ }\mu\text{m}$ and $1.5 \text{ }\mu\text{m}$ at interfaces B and A in Fig. 5(f), respectively. Thus, the photothermal confinement shows a 1.5 times higher value at interface B compared to A. We further find that L is wavelength dependent, since for an excitation at 1625 cm^{-1} the corresponding L_{1625} values amount to $3.03 \text{ }\mu\text{m}$ and $1.86 \text{ }\mu\text{m}$, respectively. This indicates a 1.7 times higher confinement at interface B compared to A. The difference in photothermal confinement for the two wavenumbers $L_{1625} - L_{1660}$ is $0.73 \text{ }\mu\text{m}$ and $0.36 \text{ }\mu\text{m}$ at interfaces B and A, respectively, which can be linked to different thermal diffusion dynamics. However, it should be considered that the slope from the PTS signal strongly depends on the diffraction limited probe spot size and thus results in a partial capture of signal from the same features in multiple pixels. In general, although the underlying biological features are smaller, the observed phenomena can confirm biochemical changes in accumulated proteins close to the membranes as well as changes in thermal diffusivity. Thus, each wavenumber excitation gives rise to a different temperature gradient, and simulations on DPPC bilayers have shown that the discontinuity in temperature, originating from the non-bonded interactions between atoms at the interfaces of bi-layers, depends on the induced temperature gradient [38]. In addition, the thermal resistivity is inversely proportional to the thermal conductivity k . The latter can be one or even two orders of magnitude higher in β sheets due to the well-knit hydrogen bond network [39] and the increased elasticity found in these structures [40]. Furthermore, the heat capacity of proteins can be altered by their secondary structure up to a factor of 3% [41], mainly due to the contribution of noncovalent interactions that rise from these structures. Thus, the overall thermal diffusivity and thermal diffusion length $R_{th} = \sqrt{4D \cdot t}$ will be affected if there is a higher accumulation of β sheets. Here, D is the thermal diffusivity and t corresponds to time interval. For the duration of 1 period $\sim 10 \text{ }\mu\text{s}$ and an average thermal diffusivity of $0.03 \text{ nm}^2/\text{ps}$ (measured in protein water interfaces) [36] we estimate a thermal diffusion length of $\sim 1 \text{ }\mu\text{m}$ at the interface. Likewise for the thermal diffusivity of water $D_{water} = 1.43 \times 10^{-7} \text{ m}^2 \cdot \text{s}^{-1}$, R_{th} is estimated around $2.3 \text{ }\mu\text{m}$. Knowing that between consecutive pump pulses, thermal relaxation occurs, this value is of the same order as the photothermal confinement derived. Taking the different biochemical composition into consideration that affect k and D , this could explain how the spatial extent

of $|\Delta\Theta|$ is $1.8\ \mu\text{m}$ at interface B compared to $0.6\ \mu\text{m}$ on interface A (\sim three times larger), see Fig. 5(f). Similarly, this affects the wavelength dependency of the difference in photothermal confinement between the two different wavenumbers $L_{1625} - L_{1660}$ is $0.73\ \mu\text{m}$ at interface B compared to $0.36\ \mu\text{m}$ at interface A (\sim two times larger). This indicates that the potential higher accumulation of β sheets near the upper membrane interface results in a larger spatial phase shift and a more significant change in the rate of heat transport across the membrane interface. Thus, both the locally induced temperature gradient across the membrane as well as the β sheet concentration relative to α helix proteins plays a pivotal role in the underlying heat dynamics.

8. Discussion

In this study, we have demonstrated that with mid-IR photothermal VIPPS imaging, high contrast from membrane interfaces can be obtained and subcellular protein signatures near the membrane regions in fibroblast cells can be chemically identified. Spectroscopic lock-in phase shifts can be observed when a material phase transition is induced [22] or when multiple absorbers with different thermal diffusion and absorption coefficients that form a natural thermal boundary between them, are being heated simultaneously [24]. In the latter case, for the value of $\Theta = 0\ \text{rad}$, the heat diffusion within the extent of the probe beam is minimized and this effect has been correlated with highest heat localization, increased resolution power and minimal thermal blurring [24]. In these biological samples, the location at which the phase crosses $0\ \text{rad}$, or is minimized, overlaps directly with the position of minimum absorption or PTS signal near the membrane region as seen clearly in Fig. 2. This allows us to conclude the presence of a thermal barrier at the interface characterized by different thermal diffusion parameters. Thus, we can directly correlate the concept of the zero-phase crossing to the existence of a thermal barrier in biological membranes. Thus, the VIPPS microscope enables visualizing sub-diffraction limited features of nano-scale dimensions in heterogeneous and complex biological samples and leads to enhanced contrast.

It has been shown that the thermal diffusivity of protein-water interfaces ($D_{\text{membrane}} = 3 \cdot 10^{-8}\ \text{m}^2\text{s}^{-1}$) [36] is one order of magnitude smaller than that of pure water ($D_{\text{water}} = 1.43 \cdot 10^{-7}\ \text{m}^2\text{s}^{-1}$). In addition, it has been discussed that the plasma membrane features an increased thermal resistivity [42,43], which would prevent heat diffusion over the time scale of a pump period ($10\ \mu\text{s}$). Similarly, the thermal conductivity of pure proteins has been shown to be lower ($\sim 0.1\text{--}0.2\ \text{W} \cdot \text{K}^{-1} \cdot \text{m}^{-1}$) compared to water ($0.6\ \text{W} \cdot \text{K}^{-1} \cdot \text{m}^{-1}$) [36], indicating that membrane structures consisting of many transmembrane proteins can support high spatial thermal gradients, compared for example to the cytoplasm, which is mainly composed of water. While an increased thermal resistivity in organelles (i.e. the nucleus) of living cells has been measured with temperature rises up to $1\ \text{K}$ between the nucleus and the cytoplasm [42], it has been discussed that living single cells under endogenous thermogenesis cannot easily maintain such a temperature variation under standard conditions [43]. However, for the fixed cells presented here, the temporary temperature increases are induced through the inherent sample absorption of the external pump light excitation. As a consequence, a stronger confinement of the heat occurs, which limits a homogenous distribution of heat across the interface. Thus, we suggest that the cell membrane can act as a thermal barrier, as noticeable from the phase signals. These effects could potentially be even more pronounced and contain more detailed features than reported here, since they can have been “diluted” by collecting averaged signals from the whole probe beam area whose dimensions exceed the biological feature sizes. However, given the nano-meter extension of the cell membrane, it is remarkable that we can visualize these changes with such detail.

Another interesting finding is related to the spectroscopic signatures associated with the imaged subcellular features. We found that the relative ratio ρ between β sheets and α helices changes in the proximity of the plasma and nuclear membrane, which is accompanied by shifts in the

measured Θ signal. These results indicate that different chemical composition expressed by the ratio ρ (e.g. the relative accumulation of β sheet structures) can result in different heat diffusion properties near membrane structures. Transmembrane proteins can contain single α helices, multiple α helices or rolled up β sheets [44]. Variations in protein conformations result in different optical and thermal properties, including absorption cross-sections and thermal diffusivities [36]. When membrane proteins undergo conformational changes, this results in membrane perturbations, which can affect the thickness and fluidity of the bilayer [45], as well as the underlying thermal properties. Having a tool that can detect these underlying chemical composition changes and link them to protein conformation, can be utilized to enhance imaging contrast and resolving power based on the reported unique thermal barrier phenomenon.

For a biological interpretation of the differences reported in the spectroscopic signatures of the Amide I band, high protein accumulations at the peak have been linked to the presence of different subcellular compartments. It has been shown that secondary structures in fibrin hydrogels, as can be found in collagen, play a crucial role in the tensile strength and elasticity of fibrin matrices whose properties enable mechanisms like wound healing [46]. Fibroblasts cells co-cultured with cancerous epithelial cells and exposed to specific growth factors express α -smooth muscle actin (α -SMA) when undergoing a phenotypic change from fibroblasts to myofibroblasts [25]. Thus, high Amide-I band accumulations have been associated with the existence of α -SMA stress fibers. However, also in eukaryotic cells, areas of high absorption in the Amide-I band have been assigned to components of the cytoskeleton, e.g. cytoskeletal filaments and granular particles up to 1.5 μm size [21]. Similarly, variations in the Amide-I band strength at 1650 cm^{-1} for different positions in the cell, from the nucleus to several particles, have been reported in general. High Amide-I expression in the nucleus was assigned to an abundance of chromatin [21]. Further, it has been shown that features in the cytoskeleton based on actin structures can result in higher protein accumulation or various organelles as Golgi apparatus, endoplasmic reticulum or mitochondria. In mammalian cells, β sheets compose the voltage-dependent anion channel (VDAC) [47]. VDAC is the most abundant protein on the mitochondrial membrane and is responsible for metabolite transport. In some cell types, mitochondria are more densely packed in the perinuclear area than throughout the cell periphery [48]. Therefore, it is possible the increase in the PTS amplitude ratio ρ between β -sheets and α -helices could be related to mitochondrial accumulation in the perinuclear area. While more detailed biological experiments are needed to identify the origin of the observed protein accumulations here, we have demonstrated that VIPPS can be applied for studying the thermal properties of protein signatures and conformation at the subcellular level. Imaging the fibroblasts within an extracellular matrix environment as a physiologically relevant medium further opens the pathway for studies of 3D fibroblast cell models based on sectioning capabilities of photothermal imaging. Studying collagen formation in fibroblast cell cultures can provide additional information and feedback on the mechanism of collagen secretion, fibrosis as well as procollagen trafficking. Having a robust label-free technique based on vibrational spectroscopy coupled with thermal diffusion analysis can further lead to interesting studies to explore fundamental biology, conduct disease analysis for pathology or address material science and chemical sample analysis in complex heterogeneous media.

9. Conclusion

This study has demonstrated for the first time how mid-infrared absorption based chemical imaging can be used to study tissue models as we are able to image the protein structures of cells embedded in a protein-rich medium with similar absorption properties, without the need for a complex sample preparation. We demonstrated that photothermal imaging with a near-infrared probe beam features the advantage that both fluorescently labeled cells as well as unlabeled cells can be analyzed and imaged with high contrast. With our unique photothermal amplitude and lock-in phase signal VIPPS imaging, we can clearly image the outer cell boundary and the

cell nucleus and achieve strong agreement with fluorescent microscope measurements. While most mid-infrared photothermal work has focused on amplitude measurements, evaluating the lock-in phase component allows us to differentiate between the intracellular and extracellular environment as well as between the cell cytoplasm and nucleus due to the varying thermal diffusion rate across the membrane interfaces. This is particularly beneficial for identifying subcellular features, since we demonstrated that the membranes act as a thermal barrier. This enabled us to determine a photothermal confinement length that can provide significant insight in quantifying heat confinement at the subcellular level. Detailed spectroscopy studies in both labeled and unlabeled fibroblast cells reveal the underlying secondary protein structures near the nuclear membrane, identifying primarily β sheet and α helix accumulation. Simultaneous dual spectral imaging of the amplitude as well as of the lock-in phase signal offers a unique tool for simultaneously determining the chemical composition of the sample and the thermal diffusion properties. By linking zero-crossing in the phase to the existence of a thermal barrier at the cell membrane, high contrast imaging and detection of photothermal phenomena associated with nano-sized features is shown. This methodology can pave the way not only for novel label-free imaging of protein structures in cell cultures but also for studying heat dynamics at the subcellular level and how they are affected by the chemical composition of cells. This can open a pathway to understand cell development cycles and the role of protein accumulations. Furthermore, it can strengthen our insights into chemical and little-studied thermal diffusion processes and what role they play for cell development cycles or for disease diagnosis.

Funding

National Science Foundation (NSF ECCS-1846659); Air Force Office of Scientific Research (FA9550-19-1-0323); National Institutes of Health (NIGMS R35 GM133616); Australian National Fabrication Facility; CSIRO Research+ Science Leader Program; CSIRO ECR (CERC) Program; ECR Grant travel award; Burroughs Wellcome Fund Career Award; Boston University Cross-Disciplinary PhD Fellowship; Nanotechnology Innovation Center, Boston University.

Acknowledgments

The authors would like to acknowledge the Boston University Cross-Disciplinary PhD Fellowship and the Nanotechnology Innovation Center at Boston University.

Disclosures

The authors declare no conflicts of interest.

See [Supplement 1](#) for supporting content.

References

1. S. E. D. León, A. Pupovac, and S. L. McArthur, "Three-Dimensional (3D) cell culture monitoring: Opportunities and challenges for impedance spectroscopy," *Biotechnol. Bioeng.* **117**(4), 1230–1240 (2020).
2. E. A. Specht, E. Braselmann, and A. E. Palmer, "A critical and comparative review of fluorescent tools for live-cell imaging," *Annu. Rev. Physiol.* **79**(1), 93–117 (2017).
3. D. Tsikritsis, A. Elfick, and A. Downes, "Raman spectroscopy of fibroblast cells from a Huntington's disease patient," *Spectrosc. Lett.* **49**(8), 535–541 (2016).
4. D. Zhang, P. Wang, M. N. Slipchenko, and J.-X. Cheng, "Fast vibrational imaging of single cells and tissues by stimulated Raman scattering microscopy," *Acc. Chem. Res.* **47**(8), 2282–2290 (2014).
5. X. Nan, J.-X. Cheng, and X. S. Xie, "Vibrational imaging of lipid droplets in live fibroblast cells with coherent anti-Stokes Raman scattering microscopy," *J. Lipid Res.* **44**(11), 2202–2208 (2003).

6. J. Shi, T. T. W. Wong, Y. He, L. Li, R. Zhang, C. S. Yung, J. Hwang, K. Maslov, and L. V. Wang, "High-resolution, high-contrast mid-infrared imaging of fresh biological samples with ultraviolet-localized photoacoustic microscopy," *Nat. Photonics* **13**(9), 609–615 (2019).
7. M. Diem, A. Mazur, K. Lenau, J. Schubert, B. Bird, M. Miljković, C. Krafft, and J. Popp, "Molecular pathology via IR and Raman spectral imaging," *J. Biophotonics* **6**(11-12), 855–886 (2013).
8. I. W. Levin and R. Bhargava, "Fourier transform infrared vibrational spectroscopic imaging: integrating microscopy and molecular recognition," *Annu. Rev. Phys. Chem.* **56**(1), 429–474 (2005).
9. R. K. Reddy, M. J. Walsh, M. V. Schulmerich, P. S. Carney, and R. Bhargava, "High-definition infrared spectroscopic imaging," *Appl. Spectrosc.* **67**(1), 93–105 (2013).
10. S. Kumar, T. S. Shabi, and E. Goormaghtigh, "A FTIR imaging characterization of fibroblasts stimulated by various breast cancer cell lines," *PLoS One* **9**(11), e111137 (2014).
11. D. Zhang, C. Li, C. Zhang, M. N. Slipchenko, G. Eakins, and J.-X. Cheng, "Depth-resolved mid-infrared photothermal imaging of living cells and organisms with submicrometer spatial resolution," *Sci. Adv.* **2**(9), e1600521 (2016).
12. Z. Li, K. Aleshire, M. Kuno, and G. V. Hartland, "Super-resolution far-field infrared imaging by photothermal heterodyne imaging," *J. Phys. Chem. B* **121**(37), 8838–8846 (2017).
13. J. M. Lim, C. Park, J.-S. Park, C. Kim, B. Chon, and M. Cho, "Cytoplasmic protein imaging with mid-infrared photothermal microscopy: cellular dynamics of live neurons and oligodendrocytes," *J. Phys. Chem. Lett.* **10**(11), 2857–2861 (2019).
14. O. Klementieva, C. Sandt, I. Martinsson, M. Kansiz, G. K. Gouras, and F. Borondics, "Super-resolution infrared imaging of polymorphic amyloid aggregates directly in neurons," *Adv. Sci.* **7**(6), 1903004 (2020).
15. I. M. Pavlovets, E. A. Podshivaylov, R. Chatterjee, G. V. Hartland, P. A. Frantsuzov, and M. Kuno, "Infrared photothermal heterodyne imaging: Contrast mechanism and detection limits," *J. Appl. Phys.* **127**(16), 165101 (2020).
16. M. Schnell, S. Mittal, K. Falahkheirkhah, A. Mittal, K. Yeh, S. Kenkel, A. Kajdacsy-Balla, P. S. Carney, and R. Bhargava, "All-digital histopathology by infrared-optical hybrid microscopy," *Proc. Natl. Acad. Sci. U. S. A.* **117**(7), 3388–3396 (2020).
17. D. Zhang, L. Lan, Y. Bai, H. Majeed, M. E. Kandel, G. Popescu, and J.-X. Cheng, "Bond-selective transient phase imaging via sensing of the infrared photothermal effect," *Light: Sci. Appl.* **8**(1), 1–12 (2019).
18. Y. Bai, D. Zhang, L. Lan, Y. Huang, K. Maize, A. Shakouri, and J.-X. Cheng, "Ultrafast chemical imaging by widefield photothermal sensing of infrared absorption," *Sci. Adv.* **5**(7), eaav7127 (2019).
19. M. Tamamitsu, K. Toda, R. Horisaki, R. Horisaki, T. Ideguchi, and T. Ideguchi, "Quantitative phase imaging with molecular vibrational sensitivity," *Opt. Lett.* **44**(15), 3729–3732 (2019).
20. M. Tamamitsu, K. Toda, H. Shimada, T. Honda, M. Takarada, K. Okabe, Y. Nagashima, R. Horisaki, and T. Ideguchi, "Label-free biochemical quantitative phase imaging with mid-infrared photothermal effect," *Optica* **7**(4), 359–366 (2020).
21. L. Quaroni, K. Pogoda, J. Wiltowska-Zuber, and W. M. Kwiatek, "Mid-infrared spectroscopy and microscopy of subcellular structures in eukaryotic cells with atomic force microscopy-infrared spectroscopy," *RSC Adv.* **8**(5), 2786–2794 (2018).
22. A. Totachawattana, M. K. Hong, S. Erramilli, and M. Y. Sander, "Multiple bifurcations with signal enhancement in nonlinear mid-infrared thermal lens spectroscopy," *Analyst* **142**(11), 1882–1890 (2017).
23. M. Selmke, A. Heber, M. Braun, and F. Cichos, "Photothermal single particle microscopy using a single laser beam," *Appl. Phys. Lett.* **105**(1), 013511 (2014).
24. P. D. Samolis and M. Y. Sander, "Phase-sensitive lock-in detection for high-contrast mid-infrared photothermal imaging with sub-diffraction limited resolution," *Opt. Express*, *Opt. Lett.* **27**(3), 2643–2655 (2019).
25. S. E. Holton, M. J. Walsh, and R. Bhargava, "Subcellular localization of early biochemical transformations in cancer-activated fibroblasts using infrared spectroscopic imaging," *Analyst* **136**(14), 2953–2958 (2011).
26. S. E. Bialkowski, *Photothermal Spectroscopy Methods for Chemical Analysis* (John Wiley & Sons, 1996).
27. S. Berciaud, D. Lasne, G. A. Blab, L. Cognet, and B. Lounis, "Photothermal heterodyne imaging of individual metallic nanoparticles: Theory versus experiment," *Phys. Rev. B* **73**(4), 045424 (2006).
28. F. Scholkmann, S. Kleiser, A. J. Metz, R. Zimmermann, J. Mata Pavia, U. Wolf, and M. Wolf, "A review on continuous wave functional near-infrared spectroscopy and imaging instrumentation and methodology," *NeuroImage* **85**, 6–27 (2014).
29. R. Nachabé, D. J. Evers, B. H. W. Hendriks, G. W. Lucassen, M. van der Voort, E. J. Rutgers, M.-J. V. Peeters, J. A. Van der Hage, H. S. Oldenburg, J. Wesseling, and T. J. M. Ruers, "Diagnosis of breast cancer using diffuse optical spectroscopy from 500 to 1600 nm: comparison of classification methods," *J. Biomed. Opt.* **16**(8), 087010 (2011).
30. J. Miyazaki, H. Tsurui, and T. Kobayashi, "Reduction of distortion in photothermal microscopy and its application to the high-resolution three-dimensional imaging of nonfluorescent tissues," *Biomed. Opt. Express* **6**(9), 3217 (2015).
31. L. Goldstein and C. Ko, "Distribution of proteins between nucleus and cytoplasm of *Amoeba proteus*," *J. Cell Biol.* **88**(3), 516–525 (1981).
32. B. Alberts, A. Johnson, J. Lewis, M. Raff, K. Roberts, and P. Walter, "Membrane proteins," *Molecular Biology of the Cell*, 4th edition (2002).
33. I. M. Pavlovets, K. Aleshire, G. V. Hartland, and M. Kuno, "Approaches to mid-infrared, super-resolution imaging and spectroscopy," *Phys. Chem. Chem. Phys.* **22**(8), 4313–4325 (2020).

34. H. Yang, S. Yang, J. Kong, A. Dong, and S. Yu, "Obtaining information about protein secondary structures in aqueous solution using Fourier transform IR spectroscopy," *Nat. Protoc.* **10**(3), 382–396 (2015).
35. L. M. Miller, M. W. Bourassa, and R. J. Smith, "FTIR spectroscopic imaging of protein aggregation in living cells," *Biochim. Biophys. Acta, Biomembr.* **1828**(10), 2339–2346 (2013).
36. A. Lervik, F. Bresme, S. Kjelstrup, D. Bedeaux, and J. Miguel Rubi, "Heat transfer in protein-water interfaces," *Phys. Chem. Chem. Phys.* **12**(7), 1610–1617 (2010).
37. A. L. Garner, M. Deminsky, V. Bogdan Neculaes, V. Chashihin, A. Knizhnik, and B. Potapkin, "Cell membrane thermal gradients induced by electromagnetic fields," *J. Appl. Phys.* **113**(21), 214701 (2013).
38. S. Youssefian, N. Rahbar, C. R. Lambert, and S. Van Dessel, "Variation of thermal conductivity of DPPC lipid bilayer membranes around the phase transition temperature," *J. R. Soc. Interface* **14**(130), 127 (2017).
39. W. Tian, M. Lin, K. Tang, J. Liang, and H. Naveed, "High-resolution structure prediction of β -barrel membrane proteins," *Proc. Natl. Acad. Sci. U. S. A.* **115**(7), 1511–1516 (2018).
40. L. Zhang, T. Chen, H. Ban, and L. Liu, "Hydrogen bonding-assisted thermal conduction in β -sheet crystals of spider silk protein," *Nanoscale* **6**(14), 7786–7791 (2014).
41. J. Gómez, V. J. Hilser, D. Xie, and E. Freire, "The heat capacity of proteins," *Proteins* **22**(4), 404–412 (1995).
42. K. Okabe, N. Inada, C. Gota, Y. Harada, T. Funatsu, and S. Uchiyama, "Intracellular temperature mapping with a fluorescent polymeric thermometer and fluorescence lifetime imaging microscopy," *Nat. Commun.* **3**(1), 705 (2012).
43. G. Baffou, H. Rigneault, D. Marguet, and L. Jullien, "A critique of methods for temperature imaging in single cells," *Nat. Methods* **11**(9), 899–901 (2014).
44. H. Lodish, A. Berk, S. L. Zipursky, P. Matsudaira, D. Baltimore, and J. Darnell, "Membrane Proteins," *Molecular Cell Biology*, 4th edition (Macmillan, 2000).
45. O. S. Andersen and R. E. Koeppe, "Bilayer thickness and membrane protein function: an energetic perspective," *Annu. Rev. Biophys. Biomol. Struct.* **36**(1), 107–130 (2007).
46. F. Fleissner, M. Bonn, and S. H. Parekh, "Microscale spatial heterogeneity of protein structural transitions in fibrin matrices," *Sci. Adv.* **2**(7), e1501778 (2016).
47. V. Shoshan-Barmatz, V. De Pinto, M. Zweckstetter, Z. Raviv, N. Keinan, and N. Arbel, "VDAC, a multi-functional mitochondrial protein regulating cell life and death," *Mol. Aspects Med.* **31**(3), 227–285 (2010).
48. T. J. Collins, M. J. Berridge, P. Lipp, and M. D. Bootman, "Mitochondria are morphologically and functionally heterogeneous within cells," *EMBO J* **21**(7), 1616–1627 (2002).